A-site strontium doping effects on structure, magnetic, and photovoltaic properties of (Bi 1-x Sr x)FeO 3-δ multiferroic ceramics

Authors: C.- S. Tu, Z.- R. Xu, V. Hugo Schmidt, T.- S. Chan, R. R. Chien, and H. Son

C.-S. Tu, Z.-R. Xu, V.H. Schmidt, T.-S. Chan, R.R. Chien, and H. Son, "A-site strontium doping effects on structure, magnetic, and photovoltaic properties of (Bi 1-x Sr x)FeO 3-δ multiferroic ceramics," Ceramics International 41, 8417-8424 (2015). doi: 10.1016/j.ceramint.2015.03.043.

A-site strontium doping effects on structure, magnetic, and photovoltaic properties of $(Bi_{1-x}Sr_x)FeO_{3-\delta}$ multiferroic ceramics

Chi-Shun Tu[a,*], Zhe-Rui Xu[a], V.H. Schmidt[b], Ting-Shan Chan[c], R.R. Chien[b], Hyungbin Son[d]

[a]*Department of Physics, Fu Jen Catholic University, New Taipei City 24205, Taiwan*
[b]*Department of Physics, Montana State University, Bozeman, MT 59717, USA*
[c]*National Synchrotron Radiation Research Center, Hsinchu 30076, Taiwan*
[d]*School of Integrative Engineering, Chung-Ang University, Seoul 156-756, Republic of Korea*

Received 2 December 2014; received in revised form 4 March 2015; accepted 9 March 2015
Available online 18 March 2015

Abstract

Raman spectroscopy, X-ray diffraction (XRD), magnetization hysteresis loop, synchrotron X-ray absorption spectroscopy, and photovoltaic effects have been measured in $(Bi_{1-x}Sr_x)FeO_{3-\delta}$ (BFO100*x*Sr) ceramics for $x=0.0$, 0.05, 0.10, and 0.15. Raman spectra and XRD reveal a rhombohedral R3c structure in all compounds. A-site Sr^{2+} doping increases fluctuations in cation-site occupancy and causes broadening in Raman modes. BFO15Sr exhibits a strong ferromagnetic feature due to reduction of Fe–O–Fe bond angle evidenced by the extended synchrotron X-ray absorption fine structure. The heterostructure of indium tin oxide (ITO) film/$(Bi_{1-x}Sr_x)FeO_{3-\delta}$ ceramic/Au film exhibit clear photovoltaic (PV) responses under blue illumination of $\lambda=405$ nm. The maximal power-conversion efficiency and external quantum efficiency in ITO/BFO5Sr/Au are about 0.004% and 0.2%, respectively. A model based on optically excited charges in the depletion region between ITO and $(Bi_{1-x}Sr_x)FeO_{3-\delta}$ can well describe open-circuit voltage and short-circuit current as a function of illumination intensity.

1. Introduction

Multiferroic $BiFeO_3$ (BFO) possesses a G-type antiferromagnetic order with a spatially modulated spin structure, which does not allow net magnetization [1]. Ferromagnetic magnetization has been observed in A-site doped $(Bi_{1-x}A_x)FeO_{3-\delta}$ (A=La, Nd, Sm, Ca, Pb, Sr, and Ba) ceramics and films [2–9]. Magnetization of the doped specimens increased significantly with radius of the doped ion. For instance, spontaneous magnetization of $(Bi_{1-x}Ba_x)FeO_{3-\delta}$ ceramics increases with increasing Ba content [6]. Magnetization hysteresis loops of $(Bi_{0.95}Sr_{0.05})FeO_{3-\delta}$ (BFO5Sr) ceramic show a weak ferromagnetism due to straightening of the Fe–O–Fe bond angle [10]. X-ray photoelectron spectroscopy and neutron diffraction of $(Bi_{1-x}Sr_x)FeO_{3-\delta}$ ($x=0.0$–0.5) ceramics synthesized using a modified gel-combustion, suggest that the $Bi^{3+}\rightarrow Sr^{2+}$ substitution causes $Fe^{3+}\rightarrow Fe^{4+}$ transformation and oxygen vacancies [10]. Structures of $(Bi_{1-x}Sr_x)FeO_{3-\delta}$ ($x=0.0$–0.5) remain in the rhombohedral R3c space group and rhombohedral distortion decreases with increasing Sr^{2+} content [10]. It was reported that Sr doping can stabilize the BFO perovskite structure [11].

BFO with various electrodes has shown photovoltaic (PV) effects and photoconductivity with potential applications [12–21]. Mechanisms, including asymmetric ferroelectric PV effect [16], domain-wall model [17], and p–n junction model [20], have been proposed to explain the PV responses. Recent PV results for the ITO/BFO ceramic/Au heterostructure show obvious dependences on thickness, illumination wavelength, and electric poling [22,23]. The PV responses were attributed to photo-excited charge carriers in the interface between ITO film and BFO ceramic using a p–n junction model [22]. BFO and ITO films have exhibited p- and n-type semiconductive behaviors with carrier densities of $n_p\sim10^{23}\,m^{-3}$ and $n_n\sim10^{26}$–$10^{27}\,m^{-3}$, respectively [20,24,25].

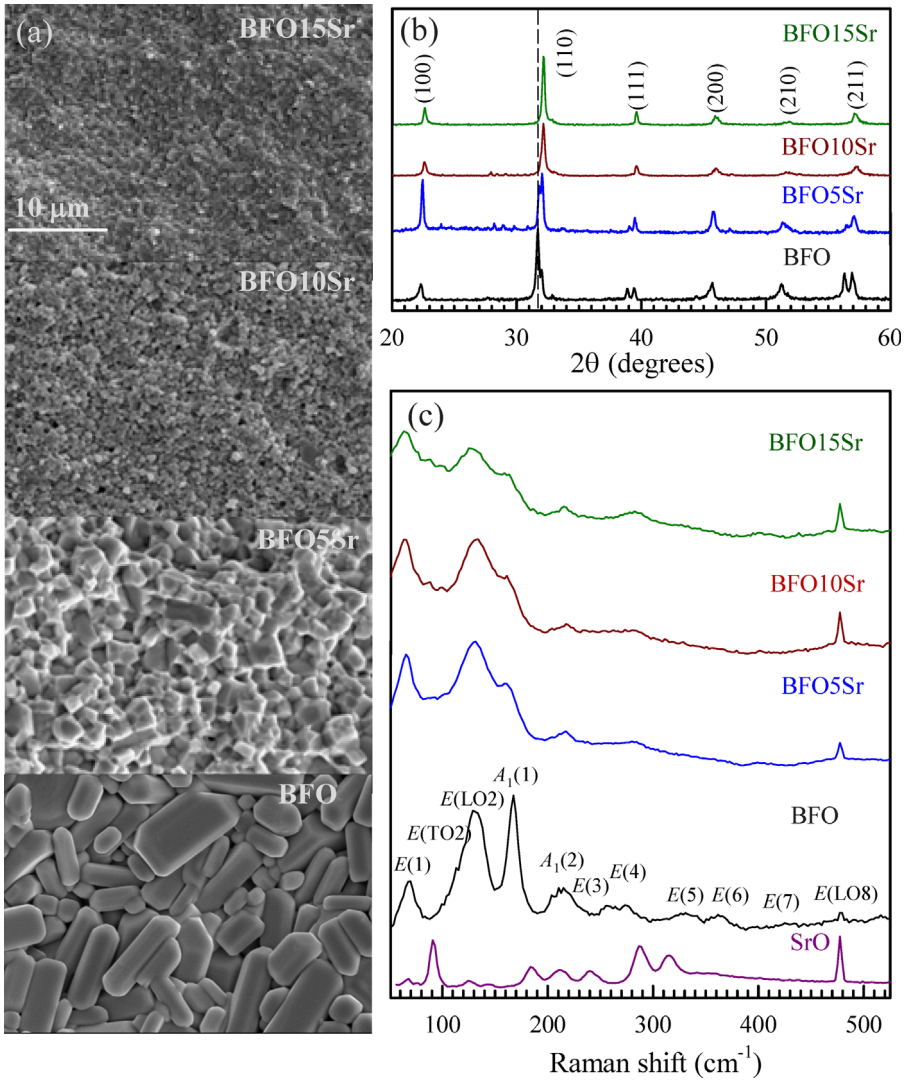

Fig. 1. (a) Grain morphologies, (b) XRD spectra, and (c) Raman spectra.

From optical transmission results, the direct optical band gaps of BFO films are in the range of 2.55–2.75 eV for rhombohedral BFO films [26–29] and 3.1 eV for quasi-tetragonal BFO films [30]. The direct optical energy gaps of $(Bi_{0.95}Sr_{0.05})FeO_{3-\delta}$ ceramics were estimated to be in the range of 1.98–2.09 eV [10]. BFO and (Mn,Sr)-doped BFO nanoparticles exhibit strong photoluminescence (PL) in the visible and IR regions [10,31]. Efficient photoluminescence emission in BFO films was identified in the range of 459–492 nm due to various electronic transitions and oxygen vacancies [28,29]. $(Bi_{0.95}Sr_{0.05})FeO_{3-\delta}$ ceramic exhibits clear photoluminescence in the visible (<550 nm) and IR (>700 nm) regions, possibly associated with oxygen vacancies [10].

Most previous studies of A-site doped BFO compounds [10,23,28,29] have focused on the photo-induced electric and optical properties. Some important physical properties still lack understanding, such as A-site doping effects on atomic vibrations and magnetic features. The aim of this work is to explore the effects of Sr^{2+} doping on Raman active modes, valences, interatomic distances, and photovoltaic responses (under blue illumination of λ=405 nm) of $(Bi_{1-x}Sr_x)FeO_{3-\delta}$ ceramics (x=0.0, 0.05, 0.10, and 0.15).

2. Experimental procedure

$(Bi_{0.95}Sr_{0.05})FeO_{2.975}$ (BFO5Sr), $(Bi_{0.90}Sr_{0.10})FeO_{2.95}$ (BFO10Sr), and $(Bi_{0.85}Sr_{0.15})FeO_{2.925}$ (BFO15Sr) ceramics were prepared by the solid state reaction method, in which Bi_2O_3, SrO, and Fe_2O_3 powders (purity $\geq$ 99.0%) were weighed respectively in 0.95:0.1:1.0, 0.90:0.20:1.0, and 0.85:0.3:1.0 ratios. The powders were mixed in an agate mortar with alcohol as a medium for more than 24 h. The dried mixtures were calcined at 800 °C (3 h) and then sintered for 3 h at 845, 865, and 885 °C for BFO5Sr, BFO10Sr, and BFO15Sr, respectively. The chemical reactions are $0.95Bi_2O_3+0.1SrO+Fe_2O_3 \rightarrow 2(Bi_{0.95}Sr_{0.05})FeO_{2.975}$, $0.90Bi_2O_3+0.2SrO+Fe_2O_3 \rightarrow 2(Bi_{0.90}Sr_{0.10})FeO_{2.95}$, and $0.85Bi_2O_3+0.3SrO+Fe_2O_3 \rightarrow 2(Bi_{0.85}Sr_{0.15})FeO_{2.925}$.

Grain morphologies and X-ray diffraction spectra of as-sintered ceramics were respectively obtained using a scanning electron microscope (SEM; Hitachi S-3400N FE-SEM) and a Rigaku Multiplex Diffractometer with wavelengths $K\alpha_1$ (1.5406 Å) and $K\alpha_2$ (1.5444 Å). Raman spectra were measured using a micro-Raman instrument (Nanobase, XperRam 200) equipped with a green laser of λ=532 nm and a TE-cooled CCD detector (1024 × 128 pixels). A high magnification objective (40 ×, 0.75 NA) was used to focus the laser to a spot of ~1 μm. To determine oxidation states and interatomic distances, the X-ray absorption near edge structure (XANES) and extended X-ray absorption fine structure (EXAFS) spectra of Fe K- and Bi L_{III}-edges were recorded in transmission mode at the 01C1 beam line at the National Synchrotron Radiation Research Center (NSRRC), Taiwan. The overall XANES spectra were normalized and calibrated by standard procedures. An analytical program "Artemis" for curve-fitting was used in the EXAFS analyses. For photovoltaic (PV) and power-conversion measurements, Au and ITO films electrodes were deposited on ceramic surfaces by dc sputtering. The thickness and illuminated area (also area of ITO film) of the samples are 0.02 cm and ~0.15 cm^2. A blue diode laser of λ=405 nm was used as the illumination source. The optical transmission of ITO film is about 80% at λ=405 nm. The open-circuit voltage (V_{oc}) and short-circuit current density (J_{sc}) were obtained as functions of light intensity.

3. Results and discussion

Grain morphologies of as-sintered ceramics are shown in Fig. 1(a), in which $(Bi_{1-x}Sr_x)FeO_{3-\delta}$ (x=0.05, 0.10, and 0.15) ceramics show different geometrical shapes from the rectangular grains in pure BFO. Grain sizes of BFO5Sr ceramic distribute in the range of 2–3 μm. Most grain sizes of BFO10Sr and BFO15Sr ceramics are smaller than 1.0 μm. The SEM morphologies suggest that grain size decreases with increasing Sr doping concentration in $(Bi_{1-x}Sr_x)FeO_{3-\delta}$ ceramics.

The X-ray diffraction (XRD) spectra of as-sintered samples are shown in Fig. 1(b). BFO5Sr shows apparent splittings in higher 2θ peaks, indicating a rhombohedral structure at room temperature the same as the pure BFO ceramic. The intense (100) and (200) peaks in BFO5Sr suggest a preferred (100) crystallographic orientation in the ceramic grains. As Sr content increases, the XRD reflections of BFO10Sr and BFO15Sr shift slightly to higher 2θ positions as indicated by the dashed line. BFO10Sr and BFO15Sr show almost no splitting in all XRD peaks, revealing a single-phase pseudo-cubic structure. This result suggests that Sr doping in BFO can reduce rhombohedral distortion. Based on the (110) reflections, the calculated lattice parameter of the pseudocubic structure is about a~3.952 Å for both BFO10Sr and BFO15Sr.

Fig. 1(c) shows micro-Raman spectra to identify the strontium effects on atomic vibration frequencies. The Raman active modes of the rhombohedral R3c structure for $BiFeO_3$ can be summarized as the irreducible representation: $\Gamma=4A_1+9E$ [32–34]. All $(Bi_{1-x}Sr_x)FeO_{3-\delta}$ (x=0.0, 0.05, 0.10, and 0.15) compositions exhibit similar Raman spectra and vibration modes, indicating the same rhombohedral R3c space group. Bi atoms participate mainly in the low-frequency modes below 170 cm^{-1} and Fe atoms are involved in vibration modes in the region of 150–270 cm^{-1} [35]. Oxygen motions strongly dominate in Raman modes above 260 cm^{-1}. The four lowest and strongest Raman vibrations can be attributed to the E(1) mode near 70 cm^{-1}, E(LO2) mode near 130 cm^{-1}, A_1(LO1) mode near 160 cm^{-1}, and A_1(LO2) mode near 220 cm^{-1} [35]. The atomic vibrations near 220 cm^{-1} mainly originate from the A_1 tilt mode of the FeO_6 oxygen octahedra. Two higher frequency Raman E(LO4) and E(LO8) modes appear respectively near 280 and 480 cm^{-1}[35], which mainly associate with atomic vibrations between the A-site atom and oxygen. As shown in Fig. 1(c), the A-site Sr^{2+} doped $(Bi_{1-x}Sr_x)FeO_{3-\delta}$ compounds exhibit broadened Raman spectra in the E(2) and A_1(1) modes, which likely result from lattice anharmonicity and from disorder consisting of fluctuations in the cation-site occupancy [35]. The A_1(1) and A_1(2) peaks are suppressed likely due to the symmetric reduction of FeO_6 oxygen octahedra resulting from Sr^{2+} doping, which could disturb the local equilibrium energy. In addition, the E(LO8) peak becomes more prominent in the Sr-doped compounds because the Sr–O vibration mode is enhanced. As shown in Fig. 1(c), the Raman spectrum of pure SrO powder exhibits a strong Raman vibration near 480 cm^{-1}.

The magnetization hysteresis loops at room temperature are shown in Fig. 2. BFO5Sr and BFO10Sr exhibit a linear antiferromagnetic behavior and are similar to BFO ceramic. The BFO15Sr exhibits a hard ferromagnetic response with a remanent magnetization of ~0.32 emu/g and coercive field of ~5×10^3 G. Figs. 3(a) and 4(a) display the Fe K- and Bi L_{III}-edges XANES spectra of $(Bi_{1-x}Sr_x)FeO_{3-\delta}$ compounds and the reference samples BFO, FeO, Fe_2O_3, and Bi_2O_3, respectively. This reveals that the valences of Fe and Bi ions in BFO and $(Bi_{1-x}Sr_x)FeO_{3-\delta}$ are +3. It also rules out the presence of other bismuth ferrite secondary phases. In brief, the heterovalent substitution of $Bi^{3+} \rightarrow Sr^{2+}$ in $(Bi_{1-x}Sr_x)FeO_{3-\delta}$ (x=0.0–0.15) does not cause $Fe^{3+} \rightarrow Fe^{4+}$ valence change.

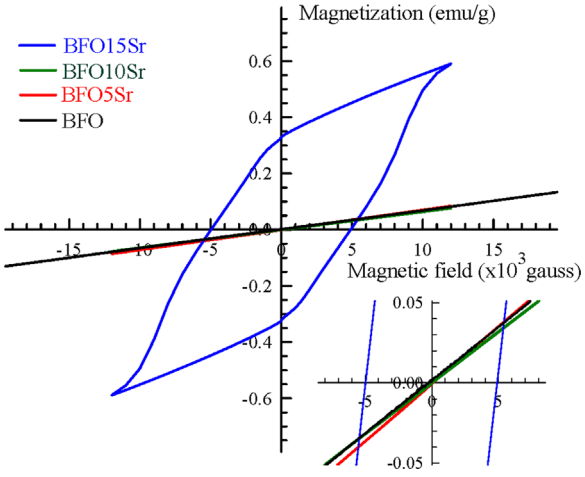

Fig. 2. Magnetization hysteresis loops at room temperature. The inset shows an enlargement of the central portions of the loops.

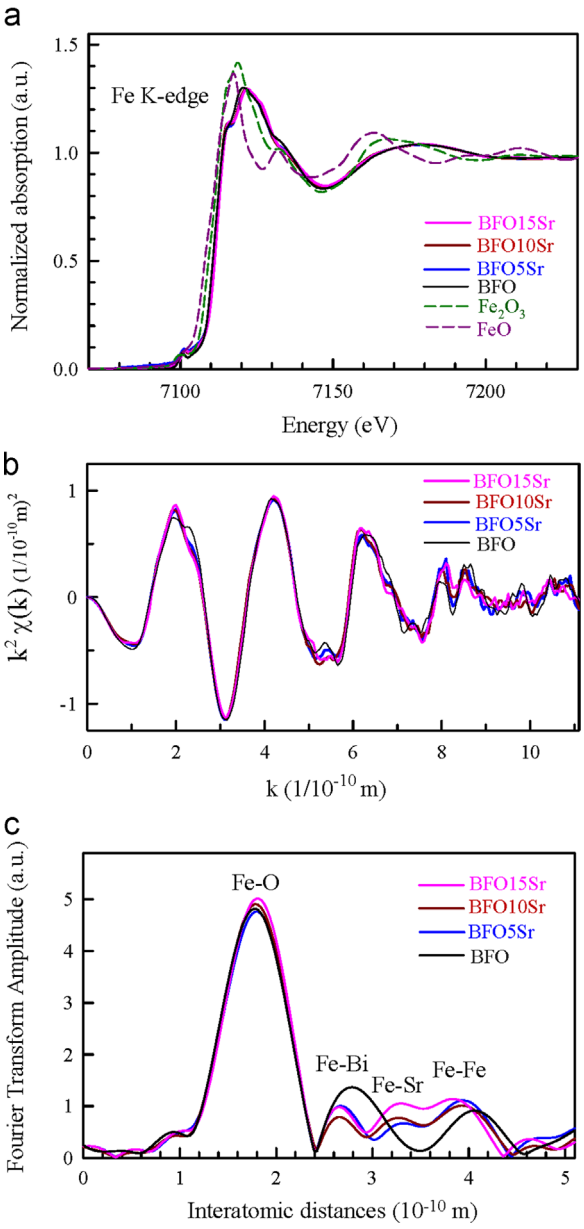

Fig. 3. (a) Fe K-edge XANES spectra, (b) EXAFS $k^2\chi(k)$ spectra in k-space, and (c) Fourier transforms of $k^2\chi(k)$ without phase correction.

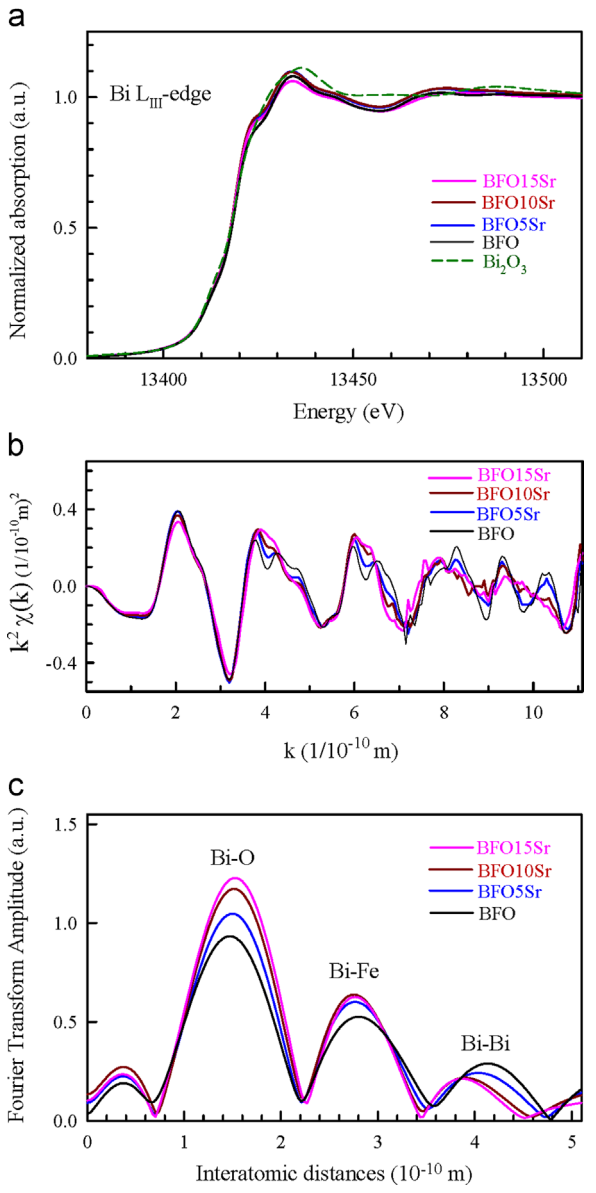

Fig. 4. (a) Bi L_{III}-edge XANES spectra, (b) EXAFS $k^2\chi(k)$ spectra in k-space, and (c) Fourier transforms of $k^2\chi(k)$ without phase correction.

The distortion of the Fe–O–Fe bond angle plays an important role in the evolution of the ferromagnetism. Figs. 3(b) and 4(b) are the extended X-ray absorption fine structure (EXAFS) oscillations (in k space), which are sensitive to the short-range structural order. As shown in Fig. 4(b), BFO15Sr shows a broader $k^2\chi(k)$ spectrum than those in BFO, BFO5Sr, and BFO10Sr in the k-space region of 8–11 (1/10^{-10} m), implying an enhanced short-range structural disorder in BFO15Sr possibly due to A-site Sr^{2+} doping. Figs. 3(c) and 4(c) are the Fourier transforms of the EXAFS $k^2\chi(k)$ spectra, which indicate that the A-site Sr^{2+} doping does not obviously change interatomic distances of Fe–O and Bi–O bonds in $(Bi_{1-x}Sr_x)FeO_{3-\delta}$ compounds. However, with the additional Fe–Sr bond in Fig. 3(c), the interatomic distances of Fe–Bi and Fe–Fe bonds in the Sr-doped compounds become shorter than that in pure BFO. The interatomic distance of the Fe–Fe bond in BFO15Sr is obviously shorter than those in BFO, BFO5Sr, and BFO10Sr. This suggests that the Fe–O–Fe bond angle (where the two Fe^{3+} are in the centers of neighboring FeO_6 octahedra) is smaller in BFO15Sr. The super-exchange coupling in the Fe–O–Fe bond prefers ferromagnetism as the Fe–O–Fe bond angle changes toward 90 degrees [36,37]. Thus, as shown in (Fig. 2), the enhancement of the ferromagnetic feature in BFO15Sr is mainly due to the smaller bond angle of Fe–O–Fe.

It is important to note that the interatomic distance of the Fe–Fe bond of neighboring FeO_6 octahedra corresponds to the unit cell size. The shorter Fe–Fe bonds in Sr-doped compounds can explain why the major (110) XRD peaks of Sr-doped compounds shift to higher angles as indicated by the dashed line in Fig. 1(b).

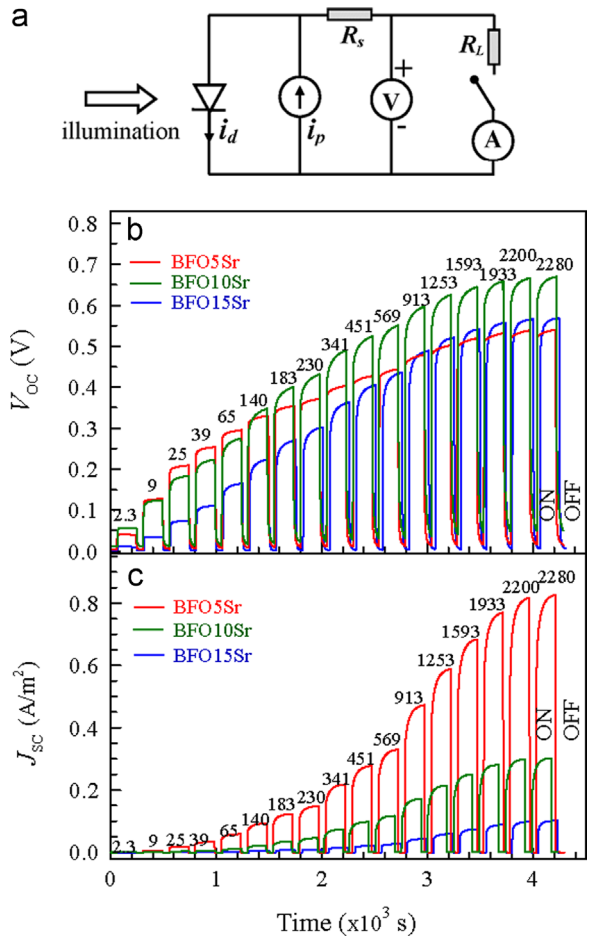

Fig. 5. (a) Experimental configuration for open-circuit voltage, short-circuit current density, *I–V* characteristic curve, and power-conversion efficiency. (b) Open-circuit voltage (V_{oc}) and (c) short-circuit current density (J_{sc}) as light was switched on and off with increasing intensity. The labeled numbers are light intensities in W/m^2.

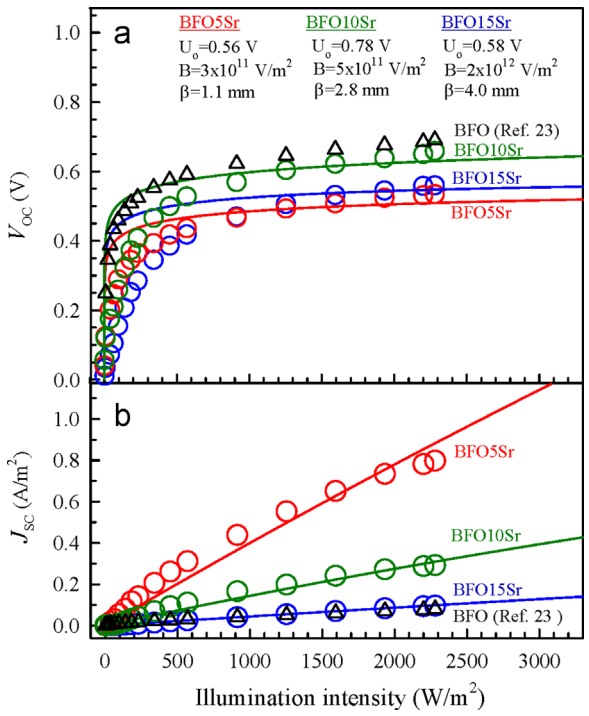

Fig. 6. (a) V_{oc} and (b) J_{sc} as a function of illumination intensity. The solid lines are the theoretical fits with parameters given in (a). The BFO data (triangle symbols) are taken from Ref. [23].

This result suggests that Sr doping can affect FeO_6 octahedra to reduce the distance between two neighboring B-site Fe ions.

Fig. 5(a) is the PV experimental configuration, in which *V* represents a voltage source for *I–V* characteristic measurement. The "diode" symbol represents the heterojunction of the n-type ITO film and p-type Sr-doped BFO ceramic. i_p, i_d, R_s, and R_L are photo-induced current, diode current, source resistance, and load resistance, respectively. For power-conversion efficiency, the relation of load current vs. load voltage was obtained by varying load resistance (R_L). Fig. 5(b) and (c) shows open-circuit voltages (V_{oc}) and short-circuit current densities (J_{sc}) of ITO/$(Bi_{1-x}Sr_x)FeO_{3-\delta}$/Au structures as the laser was switched on and off with increasing intensity (*I*). The illuminated V_{oc} and J_{sc} are plotted in Fig. 6 with increasing illumination intensity. ITO/$(Bi_{1-x}Sr_x)FeO_{3-\delta}$ ceramics/Au have larger J_{sc} and slightly smaller V_{oc} than those in ITO/BFO ceramic/Au. For instance, at $I \sim 910$ W/m^2, V_{oc} and J_{sc} are 0.62 V and 0.04 A/m^2 in ITO/BFO ceramic/Au [23], 0.47 V and 0.44 A/m^2 in ITO/BFO5Sr/Au, 0.57 V and 0.17 A/m^2 in ITO/BFO10Sr/Au, and 0.47 V and 0.04 A/m^2 in ITO/BFO15Sr/Au. These PV values are comparable with $V_{oc} \sim 0.44$ V and $J_{sc} \sim 0.25$ A/m^2 in graphene/polycrystalline BFO/Pt films at $I \sim 1 \times 10^3$ W/m^2 [15].

For photovoltaic responses, a heterojunction diode of an n-type ITO film and a p-type Sr^{2+}-doped BFO ceramic is considered for the theoretical model [21] to estimate V_{oc} and J_{sc} as a function of illumination intensity. We use Shockley's sign convention [38], that for a photodiode the sign of the output current *i* is positive. The expression of diode current i_d under a bias voltage *V* can be expressed as follows:

$$i_d = i_o\{\exp[q(V - i_d R_s)/\xi kT] - 1\}. \quad (1)$$

where ξ is diode-quality factor. To find i_o and R_s, the characteristic curves of current vs. bias voltage were measured without illumination as shown in Fig. 7. By using Eq. (1) with $q = 1.6 \times 10^{-19}$ C, $k = 1.38 \times 10^{-23}$ J/K, and $T = 300$ K, we obtained $i_o = 1 \times 10^{-17}$ A, $R_s = 4.6 \times 10^3\ \Omega$ and $\xi = 1.5$ for BFO5Sr, $i_o = 1 \times 10^{-17}$ A, $R_s = 3.2 \times 10^4\ \Omega$ and $\xi = 1.7$ for BFO10Sr, and $i_o = 1 \times 10^{-17}$ A, $R_s = 2.9 \times 10^4\ \Omega$ and $\xi = 1.6$ for BFO15Sr. ξ usually varies from 1 to 3 [39] and depends on grain size [40]. From Eq. (1), the measured current *i* can be expressed as a function of measured voltage under illumination by [21]

$$i = i_p - i_d = i_p - i_o(\exp\{[V - (i_d - i_p)R_s]q/\xi kT\} - 1). \quad (2)$$

where i_p and i_d are the photo-induced and diode currents. Through a considerable theoretical derivation presented in Ref. [21], short-circuit current (i_{sc}) and open-circuit voltage (V_{oc}) can be expressed as a function of illumination intensity, i.e.

$$i_{sc} = (U_o/R_s) - B\{i_{sc} + i_o[\exp(i_{sc}R_s q/\xi kT) - 1]\}^2\beta^2/(R_s i_I^2) \quad (3)$$

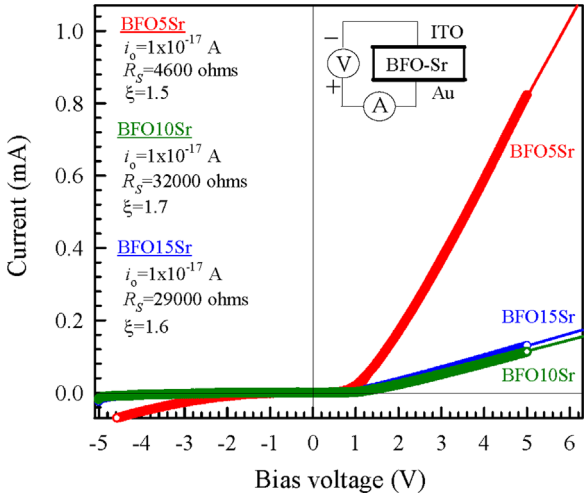

Fig. 7. Characteristic curves of current vs. bias voltage without illumination.

$$V_{oc} = U_o - Bi_o^2[\exp(V_{oc}q/\xi kT) - 1]^2\beta^2/i_I^2 \quad (4)$$

$$i_I = qS\lambda I/hc; \quad B = (qn_p/2\varepsilon_o\varepsilon_p)(1 + n_p\varepsilon_p/\varepsilon_n n_n) \quad (5)$$

where S, λ, h, and c are the illumination area, light wavelength, Planck constant, and light speed, respectively. ε_p and ε_n are the dielectric permittivities of p-type Sr^{2+}-doped BFO ceramics and n-type ITO film, respectively. n_p and n_n are the carrier densities of p-type Sr^{2+}-doped BFO and n-type ITO film, respectively. U_o is the voltage step across the depletion region without illumination. β is the attenuation length.

The solid lines in Fig. 6 are fits of J_{sc} ($=i_{sc}/S$) and V_{oc} by using Eqs. (3) and (4) with fitting parameters given in Fig. 6(a). The theoretical fits agree reasonable well with experimental results for most illumination intensities with physically reasonable parameters. The estimated carrier densities (n_p) of BFO5Sr, BFO10Sr, and BFO15Sr ceramics are respectively 7.3×10^{21}, 1.3×10^{22}, and 5.9×10^{22} m^{-3}. The estimated depletion-region widths for no illumination are $d_o \sim 1.37$, $d_o \sim 1.25$, and $d_o \sim 0.54$ μm for BFO5Sr, BFO10Sr, and BFO15Sr ceramics, respectively. The estimated optical attenuation lengths (β) are 1.1, 2.8, and 4.0 mm for BFO5Sr, BFO10Sr, and BFO15Sr ceramics, respectively. This presented model only considers the photo-excited electron–hole creation and this may cause the disagreement between experimental V_{oc} and theoretical fits at low illumination intensity as shown in Fig. 6(a). Other absorption and dissipation mechanisms, such as internal reflection by grain boundaries, oxygen vacancies, and charge recombination, may contribute to the photovoltaic responses.

Fig. 8 shows the curves of power-conversion efficiency (η) vs. load voltage (V) for several selected illumination intensities. The maximal power-conversion efficiency (η_{max}) decreases rapidly with increasing Sr^{2+} content. As shown in Fig. 8(a), the maximal power-conversion efficiency η_{max} of ITO/BFO5Sr/Au at $I \sim 1250$ W/m^2 reaches 0.004%, which is larger than $\eta_{max} \sim 0.0025\%$ in graphene/polycrystalline BFO/Pt films [15], but slightly smaller than $\eta_{max} \sim 0.005\%$ in

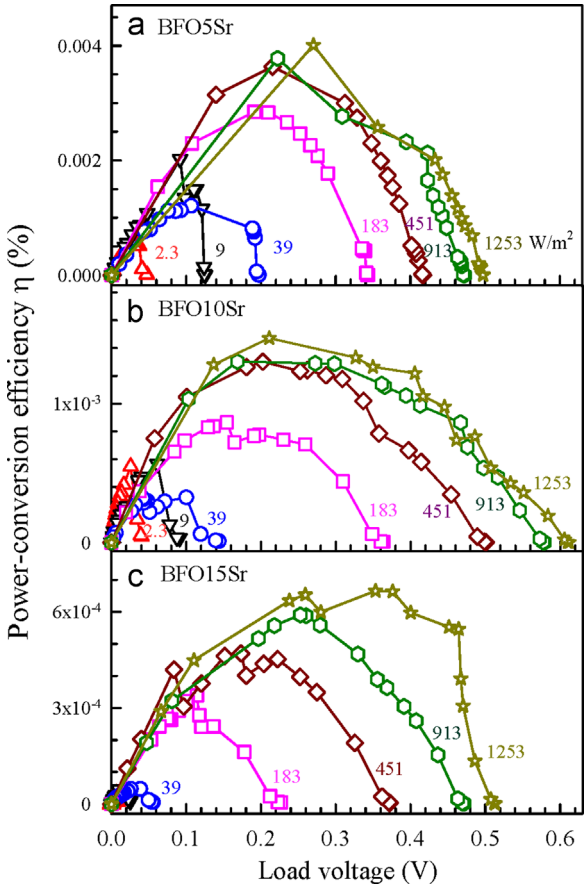

Fig. 8. Illuminated power-conversion efficiency (η) vs. load voltage. The labeled numbers are light intensities in W/m^2.

Au/polycrystalline BFO/Pt [14] and $\eta_{max} \sim 0.007\%$ in ITO/$(Bi_{0.90}Ca_{0.10})FeO_{2.95}$/Au [21]. The microstructure of Sr-doped BFO ceramics is believed to play an important role in the photovoltaic responses. The polarization direction, domain wall, and grain boundary can influence the magnitude of electric conduction [41]. As shown in Fig. 1(b), BFO5Sr exhibits a preferred (100) crystallographic orientation in the ceramic grains as evidenced by intense (100) and (200) XRD peaks, which may enhance the photocurrent under illumination due to higher ordered polarizations and grain boundaries. Strong PV effects have also been observed in the (100) oriented BFO films [20,42,43].

Fig. 9 shows the external quantum efficiencies (EQE) calculated from the short-circuit current density given in Fig. 6(b). The EQE is a measure of conversion efficiency from incident photons to electrons, i.e.

$$\mathrm{EQE} = (\mathrm{electrons}/s)/(\mathrm{photons}/s) = hfJ/q_eI. \quad (6)$$

where J, I, h, f, and q_e are current density, illumination intensity, Planck constant, light frequency, and electron charge, respectively. The maximal EQE of ITO/$(Bi_{1-x}Sr_x)FeO_{3-\delta}$ /Au decreases rapidly with increasing Sr^{2+} content. The maximal EQE in ITO/BFO5Sr/Au reach 0.2% at $I = 183$ W/m^2. The EQE (triangle symbol) for BFO ceramic was calculated from Ref. [23].

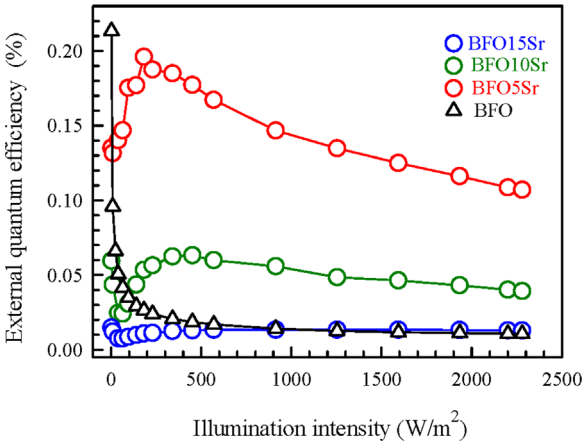

Fig. 9. External quantum efficiencies (EQE) vs. illumination intensity.

4. Conclusions

Raman spectra and XRD reveal that $(Bi_{1-x}Sr_x)FeO_{3-\delta}$ ($x=0.0$, 0.05, 0.10, and 0.15) have a rhombohedral R3c structure. Sr^{2+}-doped compounds exhibit broadened Raman spectra in the $E(2)$ and $A_1(1)$ modes, which likely result from lattice anharmonicity and from disorder produced by fluctuations in the cation-site occupancy. BFO15Sr shows a strong ferromagnetic magnetization due to reduction of the Fe–O–Fe bond angle evidenced by extended X-ray absorption fine structure (EXAFS). The heterostructure of ITO/BFO5Sr/Au exhibits a maximal power-conversion efficiency of $\eta_{max}\sim 0.004\%$ under illumination of $\lambda=405$ nm. The maximal external quantum efficiency in ITO/BFO5Sr/Au can reach 0.2% for the short-circuit case. A p–n heterojunction model for the depletion region between ITO and $(Bi_{1-x}Sr_x)FeO_{3-\delta}$ ceramics can well describe V_{oc} and J_{sc} as functions of illumination intensity.

Acknowledgment

This project is supported by the Ministry of Science and Technology, Taiwan under Project no. 103-2112-M-030-001.

References

[1] I. Sosnowska, T. Peterlin-Neumaier, E. Steichele, Spiral magnetic ordering in bismuth ferrite, J. Phys. C15 (1982) 4835–4846.
[2] S.-T. Zhang, Y. Zhang, M.-H. Lu, C.-L. Du, Y.-F. Chen, Z.-G. Liu, Y.-Y. Zhu, N.-B. Ming, X.Q. Pan, Substitution-induced phase transition and enhanced multiferroic properties of $Bi_{1-x}La_xFeO_3$ ceramics, Appl. Phys. Lett. 88 (2006) 162901.
[3] G.L. Yuan, S.W. Or, J.M. Liu, Z.G. Liu, Structural transformation and ferroelectromagnetic behavior in single-phase $Bi_{1-x}Nd_xFeO_3$ multiferroic ceramics, Appl. Phys. Lett. 89 (2006) 052905.
[4] G.L. Yuan, S.W. Or, Multiferroicity in polarized single-phase $Bi_{0.875}Sm_{0.125}FeO_3$ ceramics, J. Appl. Phys. 100 (2006) 024109.
[5] V.A. Khomchenko, D.A. Kiselev, J.M. Vieira, L. Jian, A.L. Kholkin, A.M.L. Lopes, L.G. Pogorelov, J.P. Araujo, M. Maglione, Effect of diamagnetic Ca, Sr, Pb, and Ba substitution on the crystal structure and multiferroic properties of the $BiFeO_3$ perovskite, J. Appl. Phys. 103 (2008) 024105.
[6] D.H. Wang, W.C. Goh, M. Ming, C.K. Ong, Effect of Ba doping on magnetic, ferroelectric, and magnetoelectric properties in mutiferroic $BiFeO_3$ at room temperature, Appl. Phys. Lett. 88 (2006) 212907.
[7] P. Li, Y.-H. Lin, C.-W. Nan, Effect of nonmagnetic alkaline-earth dopants on magnetic properties of $BiFeO_3$ thin films, J. Appl. Phys. 110 (2011) 033922.
[8] R. Das, K. Mandal, Magnetic, ferroelectric and magnetoelectric properties of Ba-doped $BiFeO_3$, J. Magn. Magn. Mater. 324 (2012) 1913–1918.
[9] Reetu, A. Agarwal, S. Sanghi, Ashima, Improved dielectric and magnetic properties of Ti modified $BiCaFeO_3$ multiferroic ceramics, J. Appl. Phys. 110 (2011) 073909.
[10] S.K. Mandal, T. Rakshit, S.K. Ray, S.K. Mishra, P.S.R. Krishna, A. Chandra, Nanostructures of Sr^{2+} doped $BiFeO_3$ multifunctional ceramics with tunable photoluminescence and magnetic properties, J. Phys.: Condens. Matter 25 (2013) 055303.
[11] A. Moure, J. Tartaj, C. Moure, Processing and characterization of Sr doped $BiFeO_3$ multiferroic materials by high energetic milling, J. Alloy. Compd. 509 (2011) 7042.
[12] T. Choi, S. Lee, Y.J. Choi, V. Kiryukhin, S.W. Cheong, Switchable ferroelectric diode and photovoltaic effect in $BiFeO_3$, Science 324 (2009) 63–66.
[13] C. Himcinschi, I. Vrejoiu, M. Friedrich, E. Nikulina, L. Ding, C. Cobet, N. Esser, M. Alexe, D. Rafaja, D.R.T. Zahn, Substrate influence on the optical and structural properties of pulsed laser deposited $BiFeO_3$ epitaxial films, J. Appl. Phys. 107 (2010) 123524.
[14] B. Chen, M. Li, Y. Liu, Z. Zuo, F. Zhuge, Q.F. Zhan, R.W. Li, Effect of top electrodes on photovoltaic properties of polycrystalline $BiFeO_3$ based thin film capacitors, Nanotechnology 22 (2011) 195201.
[15] Y. Zang, D. Xie, X. Wu, Y. Chen, Y. Lin, M. Li, H. Tian, X. Li, Z. Li, H. Zhu, H.T. Ren, D. Plant, Enhanced photovoltaic properties in graphene/polycrystalline $BiFeO_3$/Pt heterojunction structure, Appl. Phys. Lett. 99 (2011) 132904.
[16] W. Ji, K. Yao, Y.C. Liang, Evidence of bulk photovoltaic effect and large tensor coefficient in ferroelectric $BiFeO_3$ thin films, Phys. Rev. B 84 (2011) 094115.
[17] S.Y. Yang, J. Seidel, S.J. Byrnes, P. Shafer, C.H. Yang, M.D. Rossell, P. Yu, Y.H. Chu, J.F. Scott, J.W. Ager III, L.W. Martin, R. Ramesh, Above-bandgap voltages from ferroelectric photovoltaic devices, Nat. Nanotechnol. 5 (2010) 143–147.
[18] Y.B. Chen, M.B. Katz, X.Q. Pan, R.R. Das, D.M. Kim, S.H. Baek, C.B. Eom, Ferroelectric domain structures of epitaxial (001) $BiFeO_3$ thin films, Appl. Phys. Lett. 90 (2007) 72907.
[19] B. Kundys, M. Viret, D. Colson, D.O. Kundys, Light-induced size changes in $BiFeO_3$ crystals, Nat. Mater. 9 (2010) 803–805.
[20] S.Y. Yang, L.W. Martin, S.J. Bymes, T.E. Conry, S.R. Basu, D. Paran, L. Reichertz, J. Ihlefeld, C. Adamo, A. Melville, Y.H. Chu, C.H. Yang, J.L. Musfeldt, D.G. Schlom, J.W. Ager III, R. Ramesh, Photovoltaic effects in $BiFeO_3$, Appl. Phys. Lett. 95 (2009) 062909.
[21] C.S. Tu, C.M. Hung, Z.R. Xu, V.H. Schmidt, Y. Ting, R.R. Chien, Y.-T. Peng, J. Anthoninappen, Calcium-doping effects on photovoltaic response and structure in multiferroic $BiFeO_3$ ceramics, J. Appl. Phys. 114 (2013) 124105.
[22] C.S. Tu, C.-M. Hung, V.H. Schmidt, R.R. Chien, M.D. Jiang, J. Anthoninappen, The origin of photovoltaic responses in $BiFeO_3$ multiferroic ceramics, J. Phys.: Condens. Matter 24 (2012) 495902.
[23] C.M. Hung, M.D. Jiang, J. Anthoninappen, C.S. Tu, Photo-induced electric phenomena in antiferromagnetic $BiFeO_3$ ceramics, J. Appl. Phys. 113 (2013) 17D905.
[24] H. Kim, C.M. Gilmore, A. Piqué, J.S. Horwitz, H. Mattoussi, H. Murata, Z.H. Kafafi, D.B. Chrisey, Electrical, optical, and structural properties of indium–tin–oxide thin films for organic light-emitting devices, J. Appl. Phys. 86 (1999) 6451.
[25] M. Rottmann, K.H. Heckner, Electrical and structural properties of indium tin oxide films deposited by reactive DC sputtering, J. Phys. D: Appl. Phys. 28 (1995) 1448–1453.
[26] S.R. Basu, L.W. Martin, Y.H. Chu, M. Gajek, R. Ramesh, R.C. Rai, X. Xu, J.L. Musfeldt, Photoconductivity in $BiFeO_3$ thin films, Appl. Phys. Lett. 92 (2008) 091905.

[27] X.S. Xu, T.V. Brinzari, S. Lee, Y.H. Chu, L.W. Martin, A. Kumar, S. McGill, R.C. Rai, R. Ramesh, V. Gopalan, S.W. Cheong, J.L. Musfeldt, Optical properties and magnetochromism in multiferroic $BiFeO_3$, Phys. Rev. B 79 (2009) 134425.
[28] A. Anshul, A. Kumar, B.K. Gupta, R.K. Kotnala, J.F. Scott, R.S. Katiyar, Photoluminescence and time-resolved spectroscopy in multiferroic $BiFeO_3$: effects of electric fields and sample aging, Appl. Phys. Lett. 102 (2013) 222901.
[29] X. Chen, H. Zhang, T. Wang, F. Wang, W. Shi, Optical and photoluminescence properties of $BiFeO_3$ thin films grown on ITO-coated glass substrates by chemical solution deposition, Phys. Status Solidi A 209 (2012) 1456–1460.
[30] P. Chen, N.J. Podraza, X.S. Xu, A. Melville, E. Vlahos, V. Gopalan, R. Ramesh, D.G. Schlom, J.L. Musfeldt, Optical properties of quasi-tetragonal $BiFeO_3$ thin films, Appl. Phys. Lett. 96 (2010) 131907.
[31] X. Yu, X. An, Enhanced magnetic and optical properties of pure and (Mn,Sr) doped $BiFeO_3$ nanocrystals, Solid State Commun. 149 (2009) 711–714.
[32] P. Hermet, M. Gofinet, J. Kreisel, Ph. Ghosez, Raman and infrared spectra of multiferroic bismuth ferrite from first principles, Phys. Rev. B 75 (2007) 220102(R).
[33] J. Hlinka, J. Pokorny, S. Karimi, I.M. Reaney, Angular dispersion of oblique phonon modes in $BiFeO_3$ from micro-Raman scattering, Phys. Rev. B 83 (2011) 020101(R).
[34] J. Bielecki, P. Svedlindh, D.T. Tibebu, S. Cai, S.-G. Eriksson, Structural and magnetic properties of isovalently substituted multiferroic $BiFeO_3$: insights from Raman spectroscopy, Phys. Rev. B 86 (2012) 184422.
[35] K. Sinha, A. Mascarenhas, G.S. Horner, K.A. Bertness, Sarah R. Kurtz, J.M. Olson, Raman line-shape analysis of random and spontaneously ordered $GaInP_2$ alloy, Phys. Rev. B 50 (1994) 7509–7513.
[36] P.W. Anderson, Antiferromagnetism theory of superexchange interaction, Phys. Rev. 79 (1950) 350–356.
[37] N. Ota, Super-exchange ferromagnetic order analysis of FeO-modified graphene- nano-ribbon, J. Magn. Soc. Jpn. 38 (2014) 107–110.
[38] W. Shockley, H.J. Queisser, Detailed balance limit of efficiency of p–n junction solar cells, J. Appl. Phys. 32 (1961) 510.
[39] A.L. Fahrenbruch, R.H. Bube, Fundamentals of Solar Cells, Academic Press, New York, 1983.
[40] K. Sen, B.P. Tyagi, Diode quality factor in polycrystalline solar cells, J. Appl. Phys. 56 (1984) 1240.
[41] N.A. Spaldin., S.-W. Cheong, R. Ramesh, Multiferroics: past, present, and future, Phys. Today 63 (2010) 38–43.
[42] R. Nechache, C. Harnagea, S. Licoccia, E. Traversa, A. Ruediger, A. Pignolet, F. Rosei, Photovoltaic properties of Bi_2FeCrO_3 eptiaxial thin films, Appl. Phys. Lett. 98 (2011) 202902.
[43] A. Bhatnagar, A.R. Chaudhuri, Y.H. Kim, D. Hesse, M. Alexe, Role of domain walls in the abnormal photovoltaic effect in $BiFeO_3$, Nat. Commun. 4 (2013) 2835.